Rheological and Structural Details of Biocidal iPP-TiO_2 Nanocomposites

Cristina Serrano[1], María L. Cerrada[1]*, Marta Fernández-García[1], Jorge Ressia[2,3], Enrique M. Vallés[2]

[1]Instituto de Ciencia y Tecnología de Polímeros (ICTP-CSIC). Calle Juan de la Cierva 3. 28006 Madrid, Spain.

[2]Planta Piloto de Ingeniería Química - PLAPIQUI (UNS-CONICET). Camino La Carrindanga Km 7,
8000 Bahía Blanca, Argentina

[3]Comisión de Investigaciones Científicas de la Provincia de Buenos Aires (CIC). La Plata, Argentina

Corresponding author E-mails: mlcerrada@ictp.csic.es

Abstract

Nanocomposites obtained from incorporation of TiO_2 nanoparticles in different amounts, ranging from 0.5 to 5 wt.%, into an isotactic polypropylene (iPP) matrix are achieved via a straightforward and cost-effective melting process. These materials exhibit a powerful germicide capability over a wide variety of regular bacteria and other microorganisms widely present in the environment that cause infections and serious illness. The iPP-TiO_2 nanocomposites show similar or improved structural characteristics than those of the pure iPP matrix and aspects as important as processability and final mechanical performance seem to be not affected because of the incorporation of these TiO_2 nanoparticles. Validation of time-temperature superposition of the molten polymers is observed within the temperature range analyzed. On the other hand, the α polymorph is the one primarily attained for these specimens. Crystallinity and most probable crystallite size are slightly dependent on TiO_2 content, both increasing as oxide composition is enlarged.

Keywords:

Nanocomposites, α polymorph, rheological parameters, crystallinity, invariant.

Introduction

The use of photocatalytic semiconductor oxides has emerged as a successful technology in the struggle against biological risks to guarantee the safety of products related to food/beverage packaging or containers for biomedical/pharmaceutical materials/devices. TiO_2-Anatase is by far the most widely used photocatalyst. Under UV illumination TiO_2 generates energy-rich electron-hole pairs able to degrade cell components of microorganisms rendering innocuous products. Moreover, no weakness with respect to the microorganism nature (bacteria, virus, fungus, etc.) is known [1,2]. Consequently, its incorporation as a constituent in polymeric multicomponent materials could be a promising alternative within the field of food and drug packaging as well as medical devices.

The packaging industry can choose from an array of polymeric materials, although polyolefins (polyethylene and polypropylene) present a flexible and robust solution offering an adequate balance between performance, processability and cost to make them the industry's material of choice. The main factors that influence the final decision for a material selection are preservation, protection and safety. Packaging must protect the contents from physical damage and from external contamination, *i.e.*, microbiological contamination. It must also preserve the quality of the contents, whether for a short shelf-life of some days, or for an extended shelf-life of several months. The intrinsically inert nature of polyolefins and, specifically, of polypropylene helps to make this polymer a perfect candidate for safe food and drug packaging complying with relevant national and international regulations.

Therefore, isotactic polypropylene (iPP) has in recent years been benefited versus other more customary materials, such as cellophane, metals and paper on account of its superior puncture resistance, low sealing threshold and competitive price. Although packages processed using conventional Ziegler-Natta iPP resins provide an attractive exterior finish, they slightly obscure the clarity in appearance of the contents. The use of metallocene catalysts for its synthesis leads to iPPs with a significant improvement in clarity, this feature making metallocene iPP an ideal material for packaging in general and for food and drug packaging in particular.

The excellent biocidal capabilities exhibited by nanocomposites based on a metallocene iPP and TiO_2 have been reported in previous works [3-5], varying either the nanoparticle composition, this ranging from 0.5 to 5 wt.%, at a given compatibilizer content, or the interfacial agent fraction at a specific TiO_2 content of 2 wt.%. This striking antimicrobial activity has been also found by using an ethylene-vinyl alcohol copolymer as polymeric matrix [6-8]. The existence of energy/charge transfer(s) through these polymer/oxide interfaces and the subsequent development of new electronic states within the nanocomposite system [9] are behind this optimal germicide capability. At industrial level, the easiness of production as well as the lowest cost of new materials is a crucial aspect for their further commercialization. Very small concentrations of nanoparticles can significantly alter the phase behavior and the flow characteristics in polymeric materials.

Insight about how nanoparticles influence the associated morphological structure [10-12] and system dynamics [13-15] of polymer-nanoparticle mixtures is only beginning to emerge, and the advancement of knowledge in these areas will be a key factor to develop design rules to engineering materials with desired properties. The study of the rheological behavior of these polymeric nanocomposites with extremely good biocidal properties turns out to be necessary in order to learn how different their processability can be in comparison with that exhibited by the neat iPP homopolymer. In addition to analyze the effect of different TiO_2 contents on the rheological response of these nanocomposites, the influence of TiO_2 nanoparticles on the polymeric crystalline morphology, the viscoelastic response in the solid state and the decomposition behavior is also evaluated. Several techniques are then required for this investigation. They comprise rheological measurements, either in the molten or solid state, X ray diffraction at wide (WAXS) and small angles (SAXS), differential scanning calorimetry (DSC) and thermogravimetry (TGA).

Experimental Part

Nanocomposite preparation

The TiO_2 component (characteristic primary particle size below 10 nm) was prepared using microemulsion synthetic route by addition of titanium (IV) isopropoxide (Aldrich) to an inverse emulsion containing an aqueous phase dispersed in n-heptane (Panreac), using Triton X-100 (Aldrich) as surfactant and 1-hexanol (Aldrich) as cosurfactant. The mixture was stirred for 24 h, centrifuged, decanted, rinsed under stirring five consecutive times with methanol (twice), water (twice) and acetone (one) to eliminate any portion from the organic and surfactant media, dried at 110 ºC for 24 h and calcined at 500 ºC for 2 h.

A commercially available metallocene-catalyzed isotactic polypropylene, iPP (Basell Metocene X50081: melt flow index of 60 g/10 min at 230 °C/2.16 kg, ASTM D1238), meeting FDA requirements for food contact (Federal Regulations, 21 CFR 177.1520), was used as polymeric matrix in the preparation of these iPP-TiO_2 nanocomposites. PP-*g*-MAH, polypropylene wax partially grafted with maleic anhydride, was used as interfacial agent (Licomont® AR 504 fine grain from Clariant) in a composition of 80 wt.-% with respect to the content in TiO_2 nanoparticles. Several TiO_2 compositions have been examined: 0.5, 1, 2 and 5 wt.-%. The resultant three-component nanocomposites were labeled as iPPTix along the manuscript, being x the TiO_2 content. These nanocomposites were prepared through a straightforward melt processing in an internal mixer with volumetric capacity of 3 cm^3 at 160 ºC and at 60 rpm for 5 min. A previous TiO_2 sonication was completed in an ultrasonic device to minimize the aggregation of nanoparticles and maximize the performance of resultant nanocomposites.

Films of these TiO_2 nanocomposites were obtained by compression molding for 5 min in a Collin press between hot plates (175 °C) at a pressure of 1.5 MPa. After this, the films were rapidly quenched (at about 100 ºC/min) by refrigerating the plates of the press with cold water

Sample characterization

The antimicrobial tests were performed using an *E. faecalis* clinical isolate brs30 from human biliary. Cells were streaked from a glycerol stock onto an appropriate agar plate, grown overnight at 45 ºC, and subsequently used for photochemical cell viability assays. To study the antimicrobial activity of the titania nanomaterials, they were contacted with a solution containing microbial cells (ca.$10^{8–9}$ CFU mL^{-1}) suspended in 1 mL broth solution. The system was placed in the UV spectrometer chamber (UVIKON 930) and irradiated with a UV light of 280 nm for different periods of time. Loss of viability after each exposure time was determined by the viable count procedure on Luria-Bertani agar plates after serial dilution (10^{-2} to 10^{-5}). All plates were incubated for 24 h prior to enumeration at the temperatures above mentioned, specific for each microorganism. A minimum of three experimental runs was carried out to determine the antimicrobial activity.

The rheological characterization was carried out in small-amplitude oscillatory shear mode using a dynamic rotational rheometer from Rheometrics Inc. (Rheometrics Dynamic Analyzer RDA-II). The tests were performed using parallel plates of 25 mm in diameter, at a frequency range between 1 and 500 rad·s^{-1}, and a temperature range of 170-250 ºC. All tests were carried out at small strains in order to assure the linearity of the dynamic responses [16].

To verify this, the series of frequency sweeps were repeated twice with the same sample at different strains. Excellent agreement between these results was found in all cases.

Transmission electron microscopy was performed at room temperature in a 200 kV JEM-2100 JEOL microscope to analyse material homogeneity. Samples were cut in thin sections (50-70 nm) by crioultramicrotomy (Leica EM UC6).

The X-ray synchrotron study was performed in the soft-condensed matter beamline A2 at Hasylab (Hamburg, Germany), working at a wavelength of 0.150 nm. The experimental setup includes a specimen holder, a MARCCD detector for acquiring two-dimensional SAXS patterns (sample-to-detector distance being 260 cm) and a linear detector for 1D WAXS measurements (distance 21 cm). A sample of crystalline PET was used for WAXS calibration and the different orders of the long spacing of rat-tail cornea (L = 65 nm) were utilized for the SAXS detector. The 2D X-ray diffractograms were processed using the A2tool program developed to support beamline A2 data processing. The profiles were normalized to the primary beam intensity and the background from an empty sample was subtracted. All experiments comprise the heating of samples from 26 up to 170 ºC at 8 ºC/min. The data acquisition was done in frames of 15 s. The WAXS degree of crystallinity, f_c^{WAXS}, was determined from the X-ray diffractograms after subtraction of the amorphous profile [17].

Calorimetric analyses were carried out in a Perkin Elmer DSC7 calorimeter connected to a cooling system and calibrated with different standards. The sample weights ranged from 6 to 9 mg and the heating rate used was 8 $ºC\cdot min^{-1}$. For crystallinity determinations, f_c^{DSC}, a value of 209 $J\cdot g^{-1}$ has been taken as enthalpy of fusion of a perfect crystalline material [18]. On the other hand, the glass transition temperature, T_g, was determined as the temperature where the specific heat increment is half of the total one at the transition.

Dynamic mechanical relaxations were measured with a Polymer Laboratories MK II Dynamics Mechanical Thermal Analyser, working in a tensile mode. The storage modulus, E', loss modulus, E'', and the loss tangent, tan δ, of each sample were obtained as function of temperature over the range from –150 to 150 ºC at fixed frequencies of 3, 10, 30, 50 Hz, and at a heating rate of 1.5 $ºC\cdot min^{-1}$. To carry out these measurements, strips around 4.0 mm wide and 18 mm length were cut from the molded sheets. The apparent activation energy values were calculated on the basis of tan δ according to an Arrhenius-type equation, considering an accuracy of ± 0.5 ºC in the temperature assignment from the maxima.

The mass loss was estimated by thermogravimetry using a TA Instruments TGA Q500 equipment working under inert and oxidant atmospheres. The equipment was calibrated according to standard protocols. The sample weights ranged from 4 to 6 mg, and the heating rate was 10 ºC·min^{-1}.

Results and discussion

Compared with other biocidal agents, an excellent power for destruction of regular bacteria, as *B. stearothermophilus*, *E. coli*, *S. aureus*, *P. jadini*, and other microorganisms widely present in the environment that cause infections and serious illness, as *P. aeruginosa* and *E. faecalis*, has been found in titania nanoparticle-polypropylene nanocomposites [3-5]. As an example, Figure 1 shows this germicide activity against the *E. faecalis* Gram positive bacterium. The blank experiment in presence of the iPP matrix demonstrates the relative innocuousness of UV radiation. Incorporation of different nanoparticled TiO_2 contents has an important impact on the cell inactivation with respect to the blank test increasing the initial velocity of elimination and further decreasing the final log-reduction at the end of the experiments. Moreover, it is also observed that maximum performance is obtained using the iPPTi2 nanocomposite. In this case, an almost complete cell inactivation of the *E. faecalis* is reached, accounting for a log-reduction of near ca. 8 units. The germicide behavior exhibited by these nanocomposites is dependent on the microorganisms evaluated [3,5] but, in all cases, a significant improvement of the biocidal activity is detected with the employment of the iPPTi2 nanocomposites.

Interactions of TiO_2 with the polymer appear as a must in order to boost the biocidal action [6,9]. This conclusion is based on the evidence that no detection of inorganic domains across the film is noticed for the samples with concentrations of TiO_2 below 2 wt. %; whereas two types of zones are observed in the iPPTi5 specimen: one lacking in oxide agglomerates and another with presence of those aggregates. Regions free of oxide agglomerates are, however, dominant (70–90% of the volume).

The existence of this intimate contact between iPP and TiO_2 will also affect the whole spectrum of properties shown by these nanocomposites, including their processability and, consequently, the capability of being produced and commercialized at an industrial level. Theoretical works suggest that the nature of the particle/polymer interactions -attractive *vs*. repulsive- may play a role in the changes exhibited by the viscoelastic properties of the molten polymeric matrix [19]. A faster polymer dynamics is observed for repulsive systems compared to the one found in the pure melt and neutral systems and it is associated with a decrease in the polymer matrix density. On the other hand, the slowing of polymer dynamics described in systems with significant attractive interactions is ascribed to a dramatic reduction in mobility of adsorbed polymeric segments along the nanoparticle surface.

Figure 2 shows the master curves obtained for the storage and loss shear moduli as well as the dynamic viscosity of these nanocomposites. It is well known that bi-logarithmic plots of the isotherms of the $G'(\omega)$, $G''(\omega)$, and dynamic viscosity $\eta'(\omega)$ can be superimposed for thermo-rheologically simple materials by horizontal shifts log (a_T), along the log (ω) axis, and vertical shifts given by log (b_T) such that [16]:

$$b_T\, G'(a_T\, \omega, T) = G'(\omega, T_{ref})$$

$$b_T\, G''(a_T\, \omega, T) = G''(\omega, T_{ref})$$

$$(b_T/a_T)\, \eta'\, (a_T\, \omega, T) = \eta'(\omega, T_{ref})$$

All isotherms measured for the neat iPP and for the various iPPTix nanocomposites are superimposed in this way, allowing attainment of time-temperature master curves. In the case of pristine polymeric samples, it is expected that they should exhibit characteristic homopolymer-like terminal flow behavior, expressed by the power-laws close to $G'(\omega) \% \omega^2$ and $G''(\omega) \% \omega$ at the temperatures and frequencies at which the rheological measurements are carried out. This terminal flow zone is clearly observed from the G' and G'' representations (see Figure 2a). This response is distinct to that exhibited by other nanocomposites of iPP and *in-situ* generated TiO_2 particles [20], with composition ranging from 2.9 to 9.3 wt.%, where significant changes in the rheological behavior in the terminal region was reported even at the lowest TiO_2 content. The absence of any terminal flow zone at low frequencies and the appearance of a secondary plateau are shown in those materials. In our case, the terminal relaxation zone in the nanocomposites is, however, observed probably because of the excellent oxide/polymer contact existing at interfaces and the non-presence of important TiO_2 agglomerates, as seen in Figure 3 for the iPPTi2 nanocomposite. These features seem to suggest the breakdown of particle–particle interactions [21], allowing that conformations of macromolecular chains remain almost unaffected. Only a slight raise on the magnitude of GN and G'' compared to that found in the pristine polypropylene is observed with increasing concentration of the TiO_2 content.

The reduced curve of dynamic viscosity is depicted in Figure 2b. Viscosity rises as inorganic content does in the nanocomposites and this increase is more significant at low frequencies in the Newtonian plateau region. Consequently, η_0 values obtained by extrapolating η' to zero frequency are slightly dependent on TiO_2 composition. The rise of η_0 with increasing TiO_2 content is shown in the inset of Figure 2b. It should be mentioned that Y axis in Figure 2b is not represented in the same scale than that in Figure 2a to allow a better visualization.

The fact that these nanocomposites show an excellent biocidal activity with respect to the practically non-existing one in the neat iPP and that their viscoelastic responses in the melt are similar to those seen in the pure iPP is quite interesting since they prove an attractive biocidal specificity with practically unchanged rheological properties. This is very important from a practical point of view since the processing conditions of these iPP-TiO_2 nanocomposites should be analogous to those of the virgin iPP.

It is also mandatory to know how different TiO_2 contents affect the final crystalline structure of these nanocomposites as well as their phase transitions, relaxation processes and thermal stability. Figure 4a shows clearly the crystalline character at room temperature of the different specimens recorded in a transmission mode. The most typical and stable crystalline structure in iPPs is the monoclinic α form, and was firstly characterized by Natta and Corradini [22]. The orthorhombic γ modification, easily identified because of its characteristic (117) diffraction peak at around 20º in 2θ profiles [23], is specially favored in the case of iPP synthesized by metallocenic catalysts due to the presence of errors homogeneously distributed among the different polymer chains [24]. It can be observed in this Figure 4a that these profiles exhibit the main diffractions characteristic of the α monoclinic iPP crystalline modification [24,25]. On the other hand, it is noticeable that there is practically no evidence of the γ modification in the pristine iPP. The distinctive (117) reflection of this polymorph appears in the WAXS profiles of the different nanocomposites although in a small content. These features can be ascribed to the relatively high cooling rate used during processing of these films since the γ form is attained in other similar metallocenic iPP homopolymers when crystallization is performed at very slow rate [26]. In fact, the profiles at room temperature (depicted in the Figure 4b) obtained after crystallizing at a rate of 8ºC/min during real-time variable-temperature WAXS experiments with synchrotron radiation show the deep effect that cooling rate has on the development of this γ polymorph. In addition, it seems that the presence of TiO_2 favors this γ form and, consequently, its content increases in the nanocomposites if compared with that exhibited by iPPTi0 homopolymer. This larger development of γ phase could be ascribed in the nanocomposites to the nucleant effect that the presence of TiO_2 nanoparticles has on the crystallization of iPP macromolecules, which will be commented later on DSC results. The shift of crystallization to higher temperatures favors the formation of γ crystals [27] up to a maximum value well-above the dynamic crystallization temperature here observed.

Crystallinity of the different specimens can be estimated from the WAXS profiles. The procedure used is the following: firstly, the amount of amorphous phase has been calculated from the comparison with the diffraction profile corresponding to a totally amorphous, elastomeric, polypropylene sample, obtained in the same diffractometer and configuration [17]. In this way, the total X-ray crystallinity at room temperature is determined from the diffractograms representing the pure crystalline components of each specimen after subtracting the scaled amorphous profile. The corresponding values obtained at room temperature are listed in Table 1. The degree of crystallinity is within the range of that found in analogous quenched metallocenic iPP specimens [26-30]. Under the quenching conditions imposed during film preparation, crystallization takes place at conditions far from equilibrium and the fast cooling applied limits even more the development of crystallites and their perfection. Incorporation of TiO_2 nanoparticles has a slight effect on the degree of crystallinity reached, its normalized value increasing as TiO_2 content does (see Table 1). Therefore, intensity of the different reflections slightly rises in the nanocomposites (see Figure 4).

The results obtained by the real-time variable-temperature synchrotron radiation experiments at wide angles obtained from the first heating after processing for the pure iPPTi0 homopolymer and all the iPPTix nanocomposites are represented in Figure 5. This figure shows an improvement of crystalline structure as temperature is increased and, then, reflections become narrower in the different specimens studied. Moreover, the (101) reflection characteristic of TiO_2 anatase polymorph is observed at around 25° in these 2θ plots. Although this diffraction overlapped with other small one from iPP, it is unambiguously observed that its intensity increases as TiO_2 content is raised in the nanocomposite.

A deeper analysis of the position, width and intensity of the (110) diffraction in those real-time variable-temperature diffractograms allows us obtaining some important quantitative information. Therefore, Figure 6a represents the dependence on temperature of the position of this (110) reflection. The trend observed in the nanocomposites seems to point out a decrease of d^{110} spacing as TiO_2 content increases, the nanocomposite iPPTi2 exhibiting similar values to those shown by iPPTi0 homopolymer. This feature indicates that incorporation of very small amount of TiO_2 leads to a small distortion of the (110) plane within the crystalline lattice (iPPTi05 and iPPTi1 specimens). This change is not observed in the iPPTi2 whereas iPPTi5 presents lower d^{110} values, pointing out to a more compact crystalline morphology. The temperature variation of d^{110} is, however, very similar for the different samples, with an apparent temperature coefficient of $(4.3 \forall 0.3) \times 10^{-5}$ nm °C^{-1}. The individual values (4.3×10^{-5} nm °C^{-1} for iPPTi0, 4.0×10^{-5} nm °C^{-1} for iPPTi05 and iPPTi1, 4.1×10^{-5} nm °C^{-1} for iPPTi2 and 4.6×10^{-5} nm °C^{-1} for iPPTi5) show the influence of TiO_2 introduction on the final crystalline characteristics.

Other parameter that provides useful information is the width of the diffractions and its dependence on temperature. Figure 6b depicts the variation of this parameter for the distinct nanocomposites. Width of monoclinic (110) diffraction remains rather constant in the iPPTi0 up to around 60 ºC becoming narrower at higher temperatures as consequence of the improvement of crystallites with temperature. A very small incorporation of nanoparticles in iPPTi05 leads to a distortion of crystalline lattice, as aforementioned. The nanocomposites iPPTi1 and iPPTi2 show a similar dependence than the homopolymer whereas the lattice enhancement and, consequently, narrowness of the (110) reflection start at lower temperatures in iPPTi5.

The analysis of intensity in this (110) diffraction allows obtaining information on crystallinity changes with temperature (see Figure 6c). These values correspond to crystallinity normalized to the actual polymer content within each nanocomposite. There are small differences with increasing nanoparticle content, crystallinity increasing as TiO_2 content does. The location of the melting of these crystalline entities can be estimated by derivation from this temperature dependence, as shown in Figure 6d. The numerical values are listed in Table 1.

The real-time variable-temperature Lorentz-corrected SAXS profiles corresponding to the first melting process of the polymeric component in the different nanocomposites are shown in Figure 7. It has to be commented that a periodicity peak is additionally observed after melting of the iPP polymeric matrix. This correlation peak is ascribed to a characteristic spacing between TiO_2 nanoparticles [20]. Looking at Figure 7, a clear long spacing is seen for all of the specimens after subtracting the TiO_2 correlation peak. An important shift to lower 1/d values of the peak related to the long spacing with temperature is observed in all of these specimens, independently of TiO_2 content, associated with the improvement of the iPP crystalline morphology by effect of temperature and, then, the thickening of its crystallites. Further information can be obtained from these profiles by analysis of the relative SAXS invariant (see Figure 8a). This is a magnitude used in the lamellar stack model theory of semicrystalline polymers which is directly related to the electron density differences between the two phases (amorphous and crystalline), so that it has rather important variations during crystallization, recrystallization or melting processes in semicrystalline polymers [31-33]. Data prove the existence of different regions: an initial one, up to around 55 ºC, where a very small increase of the SAXS invariant is seen; a second zone, between 55 ºC to around 130 ºC, with an important increase of invariant followed by a small diminishment at the end of this interval; and a final one characterized by a primary and sharp decrease, related to the main melting process.

These distinct regions can also be observed from the values of the most probable long spacing as function of temperature, deduced from the Lorentz-corrected SAXS profiles, as observed in Figure 8b. The first one, up to around 55 ºC, where the long spacing is almost constant; a second region, between 55 ºC to around 130 ºC, with a moderate increase of L; and a final one, with a very important thickening, this being ascribed to a considerable melting-recrystallization phenomena.

It is also noticeable from Figure 8b the development of thicker crystallites in the nanocomposites with respect to those existing in the iPP matrix probably due to the nucleant effect performed by TiO_2 nanoparticles. This assumption can be confirmed once long spacing, L^{SAXS}, is determined taking the values of total WAXS crystallinity, f_c^{WAXS}. The most probable crystallite size in the direction normal to the lamellae, l_c, can be estimated by assuming a simple two-phase model, *i.e.*, $l_c = f_c^{WAXS} \times L^{SAXS}$. The results for l_c are also listed in Table 1, a slight increase being observed as TiO_2 content is raised in the nanocomposites. On the other hand, information on melting temperature is also obtained from the corresponding derivatives of the relative invariant, as can be deduced from Figure 8a. The agreement with those determined from the WAXS profiles is really good, as can be seen.

The crystalline nature of these nanocomposites can be also figured out from calorimetric results represented in Figure 9a and b for the melting and crystallization processes respectively. An endothermic peak ascribed to the melting process of the α form is exhibited as seen in Figure 9a. We should keep in mind that this α polymorph is practically the unique one developed in these as-processed Q specimens, as deduced from WAXS diffractograms. However, two melting processes seem to be merged in the homopolymer and the endotherm observed in the nanocomposites is rather asymmetric. These features are related to the melting-recrystallization phenomena of these α crystallites, which become so important at high temperatures. In addition to these melting-recrystallization phenomena, the existence of two overlapped endotherms could be also due to melting of other polymorph or to the melting of two different crystallite populations. Nevertheless, those assumptions are not accomplished in these materials since WAXS profiles do not show development with temperature of an important content of other polymorph different than the α form and SAXS peaks do not point out the presence of two distinct crystallite populations. On the contrary, both WAXS and SAXS results confirm the improvement on temperature of crystalline structure through melting-recrystallization processes, as clearly seen in Figures 6b and 8a.

Another aspect deduced from these melting curves is the enthalpy of melting (see Table 1), and, consequently, the DSC crystallinity if the enthalpy of melting for the 100% crystal is known. If the widely used value [18] of 209 J g^{-1} is considered as enthalpy of fusion of a perfect crystalline material, the DSC crystallinity variation is that reported in Table 1. As previously observed from WAXS results, the values for the nanocomposites are slightly higher than that found in the iPPTi0 sample and there are not significant differences as TiO_2 content increases in the specimens.

Figure 9b shows the crystallization process for the different samples. It is clear the nucleant effect that incorporation of TiO_2 has on the iPP matrix. Consequently, crystallization temperature, T_c, is moved to higher temperature (see Table 1). The nucleant influence that the highest content of TiO_2 exerts (sample iPPTi5) is, however, less significant than that observed in the nanocomposites with lower TiO_2 composition. This feature might be ascribed to the presence of oxide agglomerates in iPPTi5, which are not observed in the other nanocomposites with lower contents, fact that can minimize the nucleant effect of the nanoparticles.

Figure 10 shows the results related to the thermal stability of iPPTi0 and the different nanocomposites under inert and oxidant conditions. Looking first at curves achieved under a nitrogen atmosphere (Figure 10a), it can be said that degradability is not affected by incorporation of oxide nanoparticles. Degradation seems to take place in a unique stage (Figure 10b) and the TiO_2 content can be estimated from residual mass at the end of the experiment. A good agreement was found if compared with the theoretical values: 0.6, 1.1, 1.9 and 4.9 for the iPPTi05, iPPTi1, iPPTi2 and iPPTi5, respectively. The picture significantly changes when thermal stability is evaluated in an oxidant environment (Figure 10c). In this case the degradation mechanism is more complex and takes place in several steps (Figure 10d). Also, the presence of TiO_2 nanoparticles favors degradability and the temperature of maximum degradation is shifted toward lower values than that corresponding to the homopolymer. Nevertheless, the onset of degradation in the nanocomposites is moved to higher temperatures about 20 ºC, this means that the onset of the degradation process is postponed with the incorporation of TiO_2. These features derived from the TiO_2 catalytic effect could have a high interest from an industrial and commercial standpoint.

After assessing their excellent biocidal properties, the constancy in processability conditions, the crystallite characteristics developed during film preparation as well as the influence of nanoparticles in the thermal degradability for these nanocomposites with different TiO_2 contents, the study of their viscoelastic behavior in solid state is essential to learn the final mechanical response. Therefore, Figure 11 shows the viscoelastic mechanisms that occur in a broad temperature interval, from -150 to 150. Three processes are observed in the plots of loss magnitudes, tan δ and E'', labeled as α, β and γ in order of decreasing temperatures. The α relaxation is related to motions within the polymer crystalline phase, especially to defect diffusion [34]. The mechanism that takes place at around 0 ºC (β process) is ascribed to generalized motions of long chain segments that occur along the glass transition. The cooperative nature of this movement explains the important decrease in E' found in this temperature range. The other relaxation process observed at temperatures lower than that related to cooperative motions is labeled as γ and is associated with rotational motions of methyl groups from polypropylene. It does actually appear as a shoulder and not as a well-defined peak even in the iPP homopolymer (see Figure 11).

Due to the partial overlap of the β and γ relaxations, the separation of the loss response into the different process contributing to the overall viscoelastic spectrum is rather convenient to estimate more accurately the location of the different relaxations. With this purpose, the deconvolution of tan δ magnitude into three distinct relaxations was performed. The tan δ response has been considered as composed by three distinct Gaussian curves, one for each observed relaxation process (also loss modulus curves can be fitted to this type of mathematical functions). Such a deconvolution does not have a theoretical basis that can explain satisfactorily the shape of the dependence of tan δ (or loss modulus) on temperature though some factors that can influence it are known. A method of curve deconvolution [35] has been proposed to analyze the dynamic mechanical loss curves in the region of the glass transition of several polymers, confirming the validity of this empirical approximation. In addition, it was shown that a Gaussian function provided the best fitting. This method constitutes a useful tool to determine the peak positions whether a good overall fitting is attained over the whole experimental temperature range measured.

The results obtained from this procedure are listed in Table 2. In view of these results we may conclude that the incorporation of TiO_2 nanoparticles does not have a remarkable effect on the location and intensity of the γ and α secondary relaxations. However, a shift to higher temperature with oxide content is seen for the primary β process. Regarding the elastic component of Young´s modulus, the values for the different specimens are also similar at different temperatures. Stiffness in the solid state is not significantly affected by introduction of small contents in nanoparticles. This means that the nanocomposites maintain the good mechanical performance exhibited by their polymeric iPP matrix.

Conclusions

Several iPP/TiO_2 nanocomposites exhibiting an extraordinary power for destruction of numerous microorganisms were prepared via a straightforward and cost-effective approach. These polymers show similar or improved structural characteristics than those of the pure iPP matrix and aspects as important as processability and final mechanical performance are not affected because of the incorporation of these TiO_2 nanoparticles. Time-temperature superposition principle is validated for all of the nanocomposites and Newtonian viscosity slightly increases as TiO_2 content is enlarged in the final material. The quenched films primarily develop the α polymorph, although the presence of nanoparticles seems to favor somehow the minor appearance of the orthorhombic γ lattice, probably because of their nucleant effect and, consequently, the shift of crystallization to slightly higher temperatures. On the other hand, crystallinity and most probable crystallite size tend to rise as TiO_2 content increases. The presence of these nanoparticles does not affect the degradability of the nanocomposites performed in an inert environment, although it has a favorable effect under oxidant conditions since the beginning of degradation is postponed and the temperature of maximum degradation is slightly decreased. Accordingly, new functional polymeric nanocomposites with tailored and precise properties can be prepared without increasing their production costs.

Acknowledgements:

The authors are grateful for the financial support of Ministerio de Ciencia e Innovación (project MAT2010-19883). J. Ressia and E. Vallés acknowledge the financial support from CONICET, FONCyT and UNS. Ms. C. Serrano is also grateful to Ministerio de Ciencia e

Innovación for her FPU predoctoral grant. The synchrotron work leading to these results has received funding from the European Community's Seventh Framework Programme (FP7/2007-2013) under grant agreement n° 226716. We thank the collaboration of the Hasylab personnel in the soft-condensed matter beamline A2, especially Dr. S. S. Funari.

Table 1. Normalized crystallinity (f_c^{WAXS}), most probable long spacing (L^{SAXS}) and most probable crystallite size (l_c) estimated at room temperature; melting temperature determined from WAXS, SAXS and DSC measurements (T_m^{WAXS}, T_m^{SAXS}, and T_m^{DSC} respectively); melting enthalpy (ΔH_m), overall crystallinity degree (f_c^{DSC}) and crystallization temperature (T_c) estimated from DSC experiments for the different specimens[a]

Sample	$\mathbf{f_c^{WAXS}}$	$\mathbf{T_m^{WAXS}}$ (ºC)	$\mathbf{L^{SAXS}}$ (nm)	$\mathbf{T_m^{SAXS}}$ (ºC)	$\mathbf{l_c}$ (nm)	$\mathbf{\Delta H_m^{DSC}}$ (J/g)	$\mathbf{T_m^{DSC}}$ (ºC)	$\mathbf{f_c^{DSC}}$	$\mathbf{T_c^{DSC}}$ (ºC)
iPPTi0	0.54	143	10.2	142	5.5	98	139.0	0.47	115.5
iPPTi05	0.55	143	11.3	142	6.2	102	141.0	0.49	117.0
iPPTi1	0.56	144	11.3	143	6.3	105	139.5	0.50	117.5
iPPTi2	0.56	143	11.2	143	6.3	105	139.5	0.50	117.5
iPPTi5	0.57	143	11.4	144	6.5	105	140.5	0.50	116.5

[a] Estimated errors: temperatures ± 0.5 ºC; enthalpies ± 4 J g^{-1}

Table 2. Relaxation temperatures (tan δ basis, at 3 Hz) for the different processes and storage modulus values at different temperatures found in the iPPTi0 homopolymer and its nanocomposites with different TiO_2.nanoparticle contents.

Sample	**T_γ** (ºC)	**T_β** (ºC)	**T_α** (ºC)	**$EN_{-100\,^{\circ}C}$** (MPa)	**$EN_{25\,^{\circ}C}$** (MPa)	**$EN_{100\,^{\circ}C}$** (MPa)
iPPTi0	-72.0	0.0	67.0	4900	1800	315
iPPTi05	-70.0	-2.5	69.0	4700	1650	310
iPPTi1	-70.0	1.5	69.5	4700	1800	310
iPPTi2	-70.0	2.0	68.5	5000	1800	320
iPPTi5	-70.0	4.0	68.5	4700	1650	310

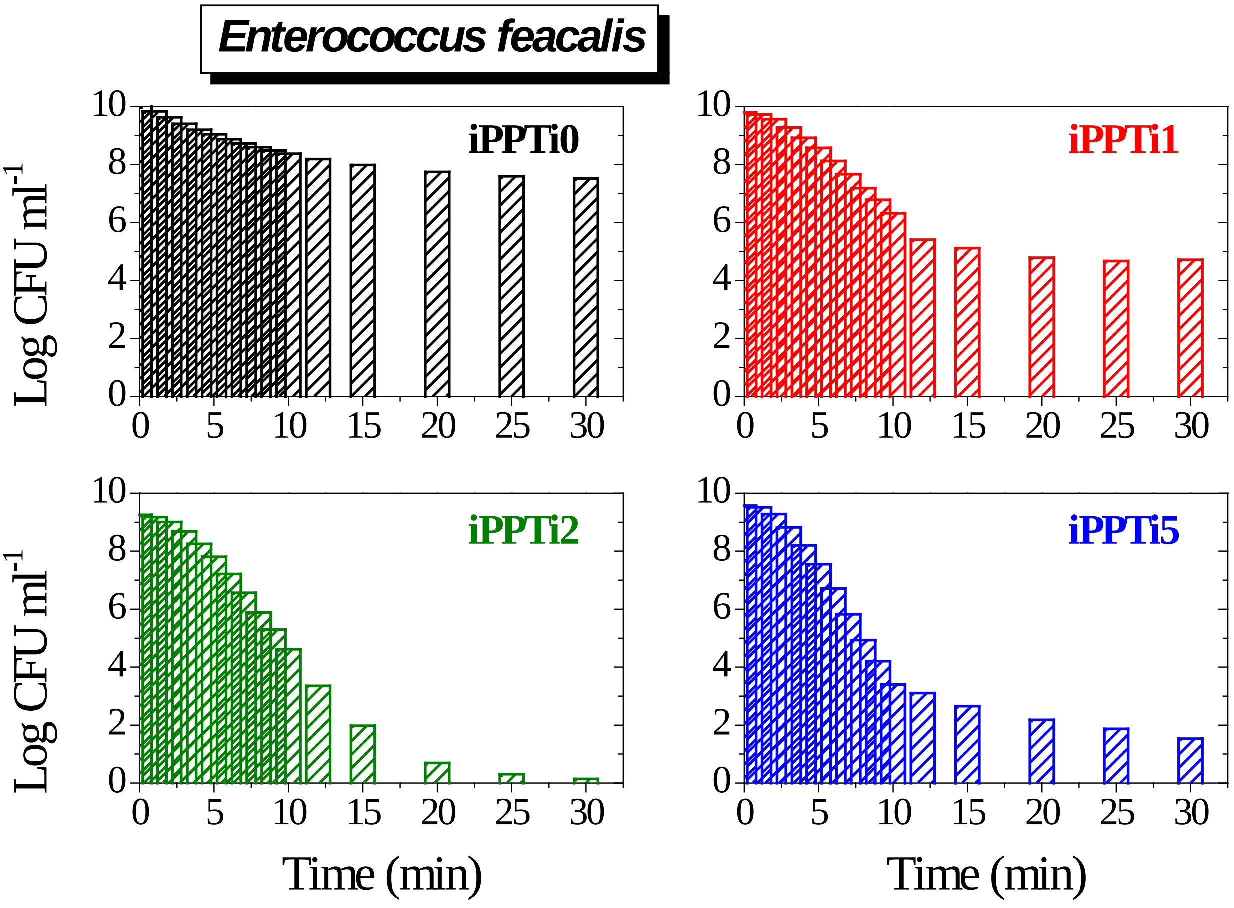

Figure 1. Process come-up logarithmic reduction of microorganism population suspended in LB medium. Survival curves of *E. feacalis* as a function of irradiation time for iPP control and iPPTix samples [5]. Values are obtained from three different measurements

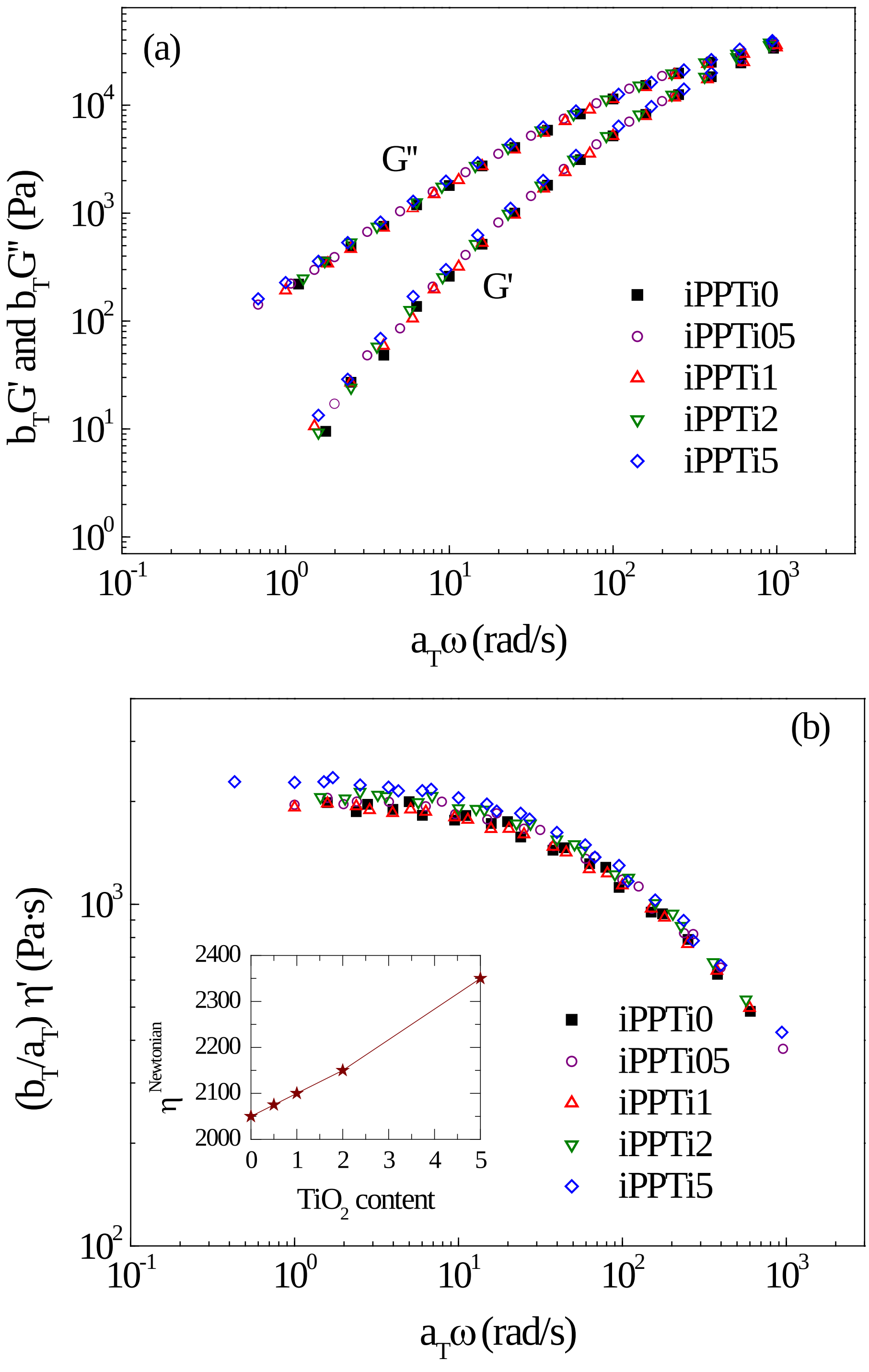

Figure 2. (a) Reduced frequency dependence of storage modulus, G´(ω) and loss modulus, G″(ω) and (b) of dynamic viscosity ((b_T/a_T) η´) observed in the metallocene iPP and its nanocomposites with TiO_2.

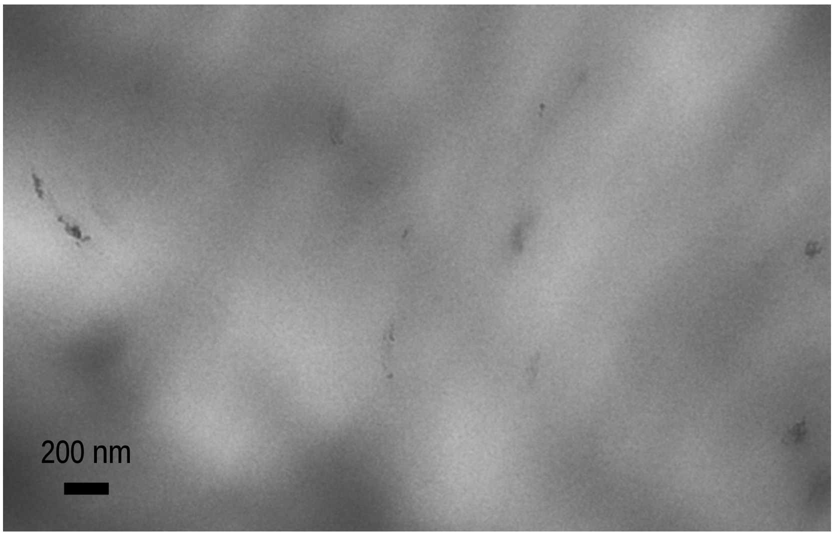

Figure 3. TEM micrograph of the iPPTi2 nanocomposite.

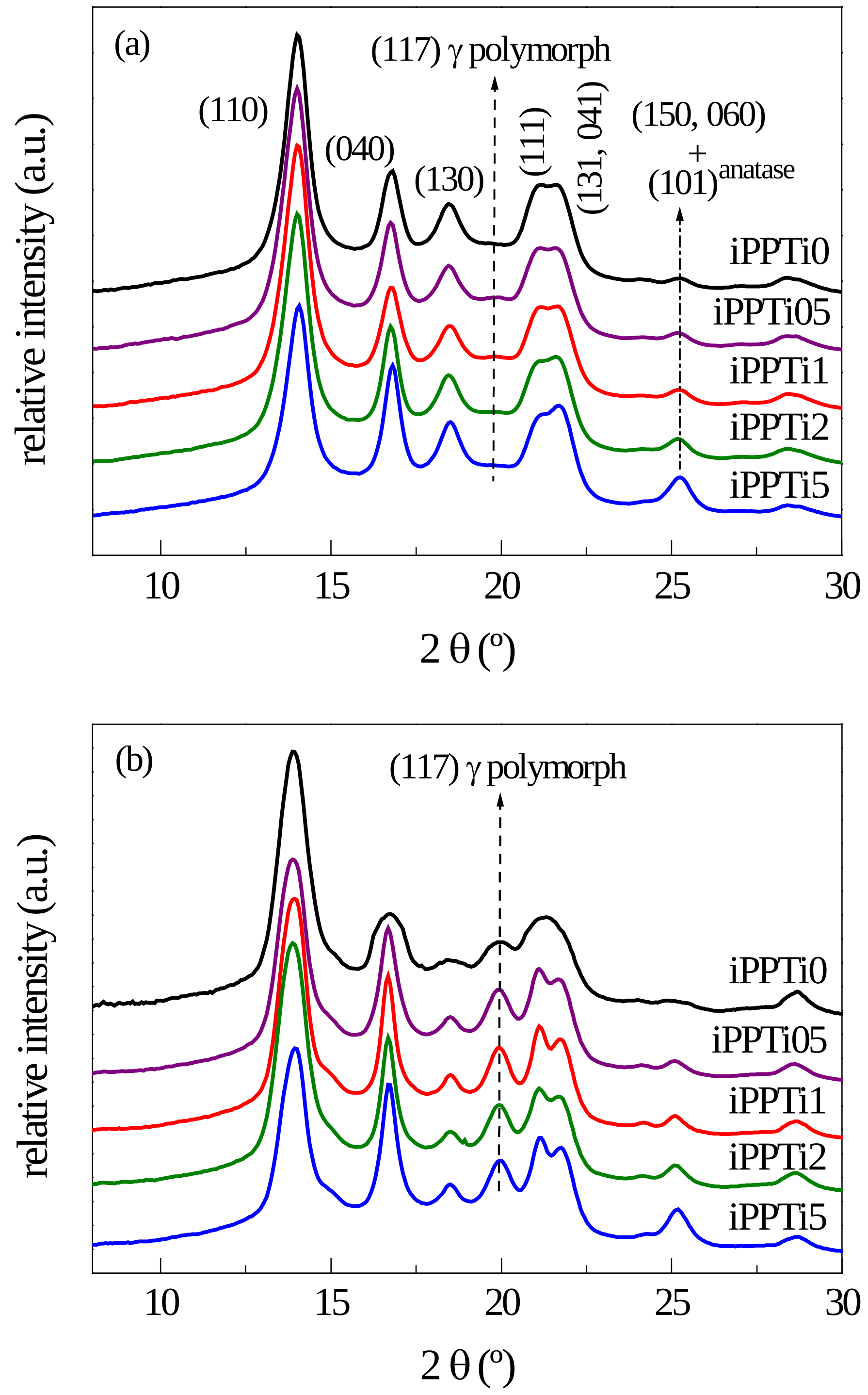

Figure 4. WAXS diffraction patterns of pure iPP and the different nanocomposites at room temperature: (a) quenched films as processed and (b) samples crystallized at 8 ºC/min after their first heating.

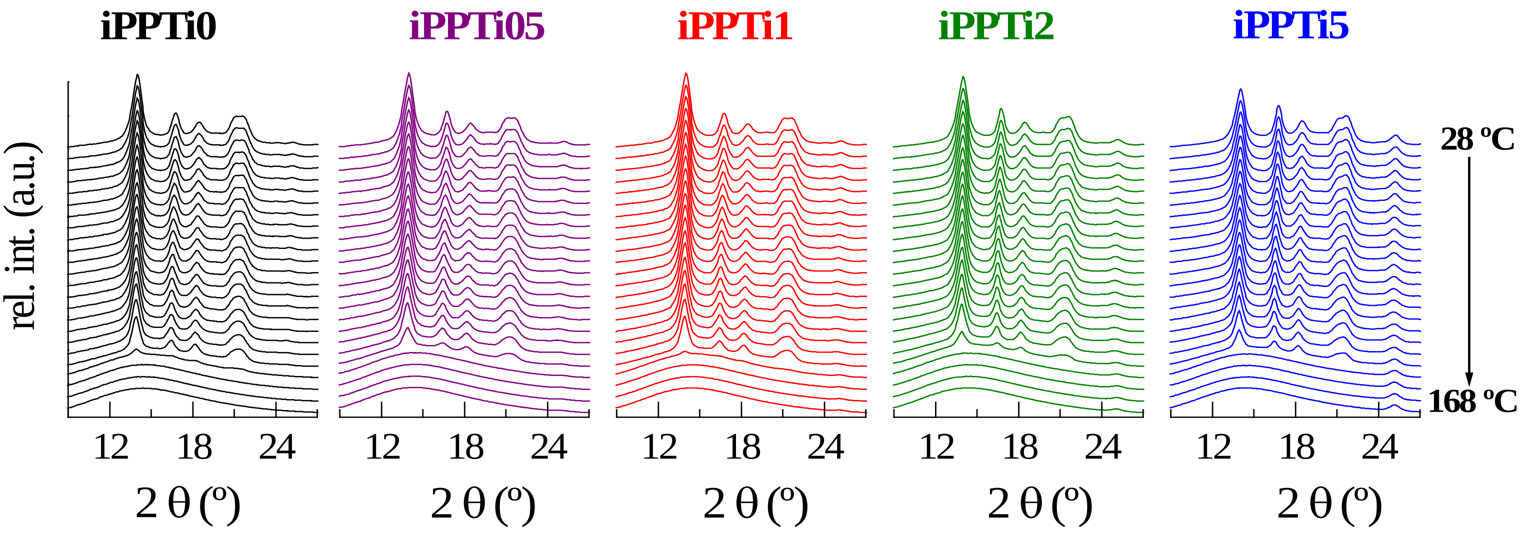

Figure 5. Real-time variable-temperature WAXS profiles obtained with synchrotron radiation for all the quenched samples as processed in a melting experiment at 8 ºC/min. Only one every three frames is plotted for clarity.

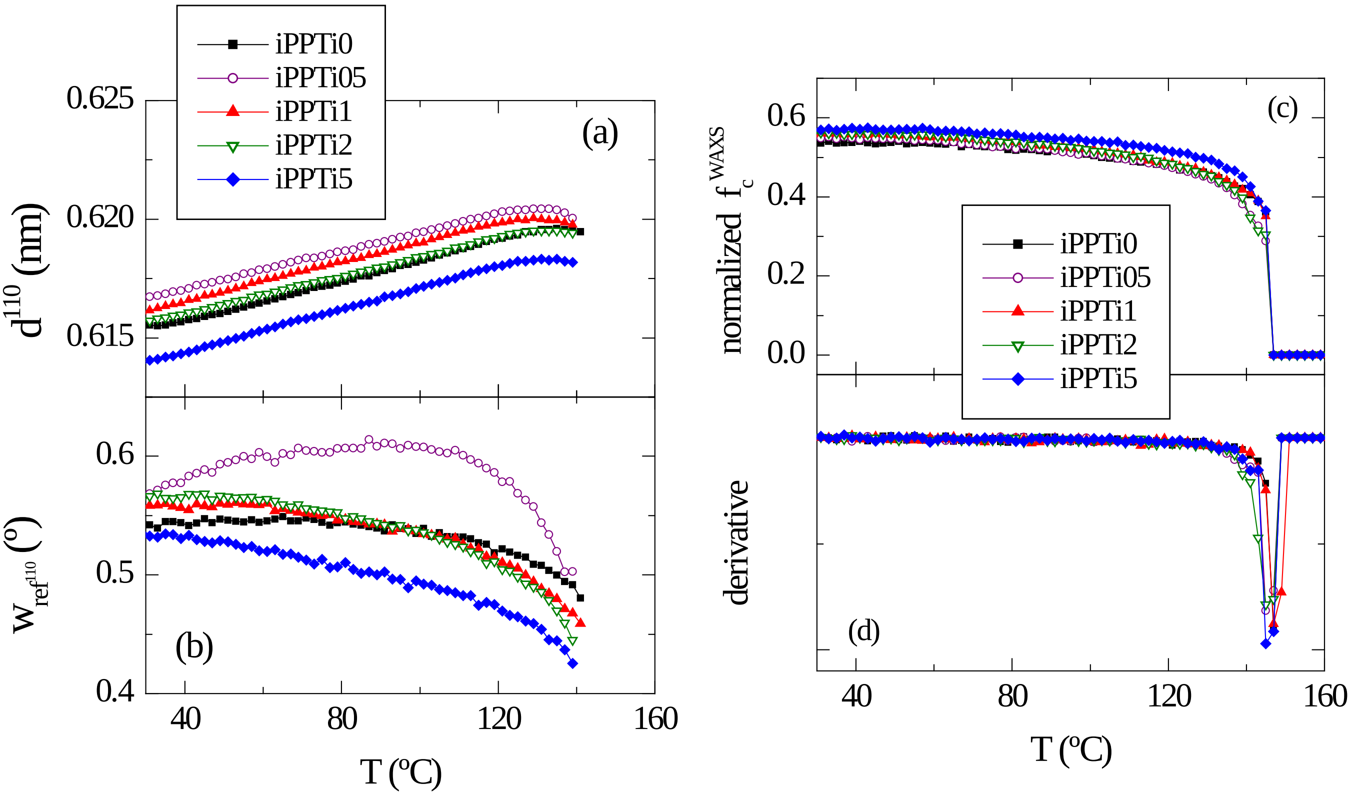

Figure 6. Temperature dependence, on melting, for the (110) monoclinic reflection of: (a) peak spacing; (b) the width at half height of this diffraction; (c) normalized crystallinity determined from it; and (d) crystallinity derivative corresponding to the neat homopolymer and its nanocomposites.

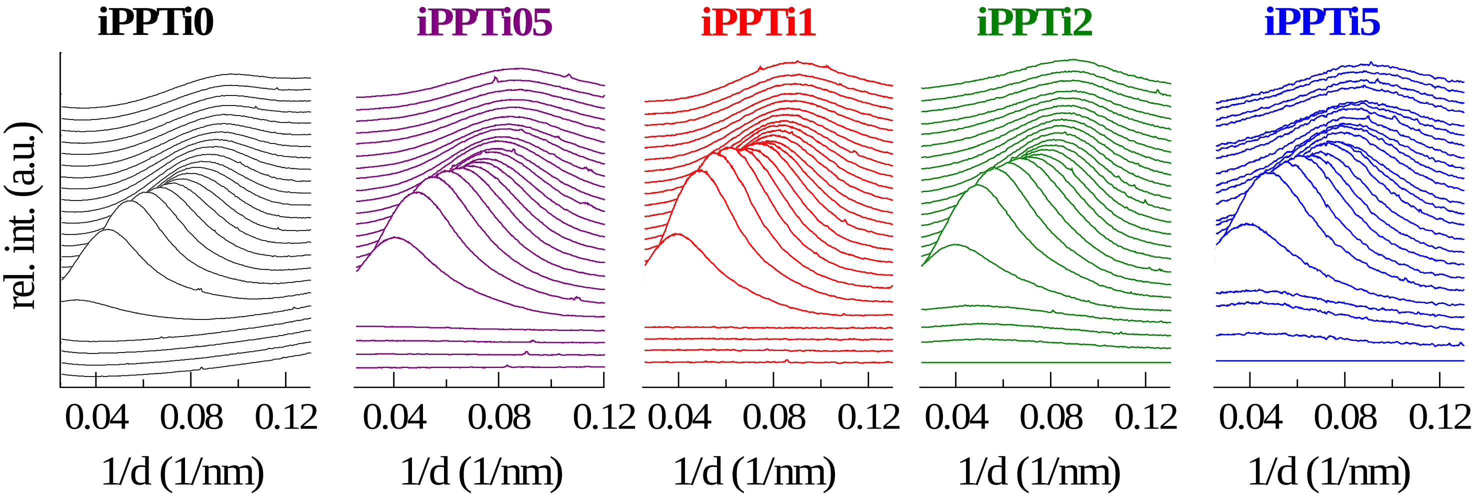

Figure 7. Real-time variable-temperature Lorentz-corrected SAXS profiles obtained with synchrotron radiation for all the quenched samples as processed in a melting experiment from 28 to 168 ºC at 8 ºC/min. Only one every three frames is plotted for clarity.

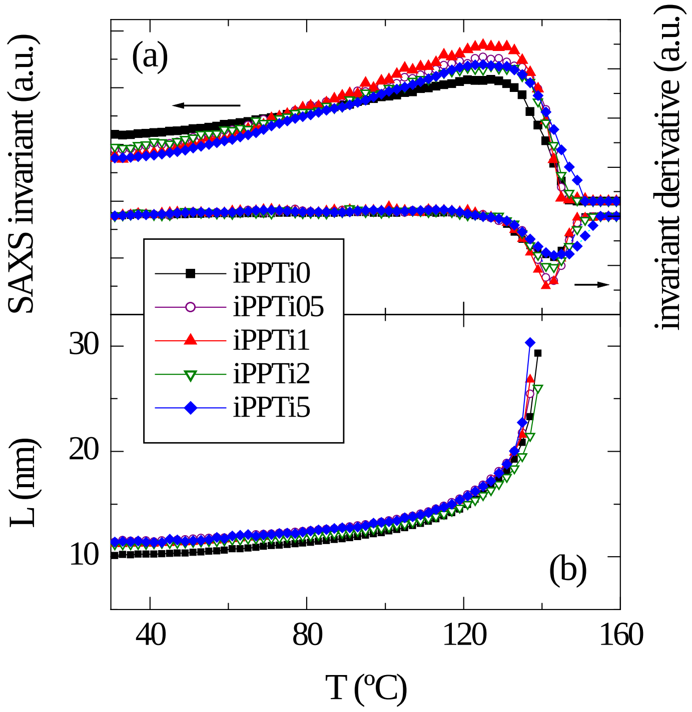

Figure 8. Temperature dependence, on melting, of (a) the SAXS relative invariant and its derivative and (b) most probable long spacing corresponding to the neat homopolymer and its nanocomposites.

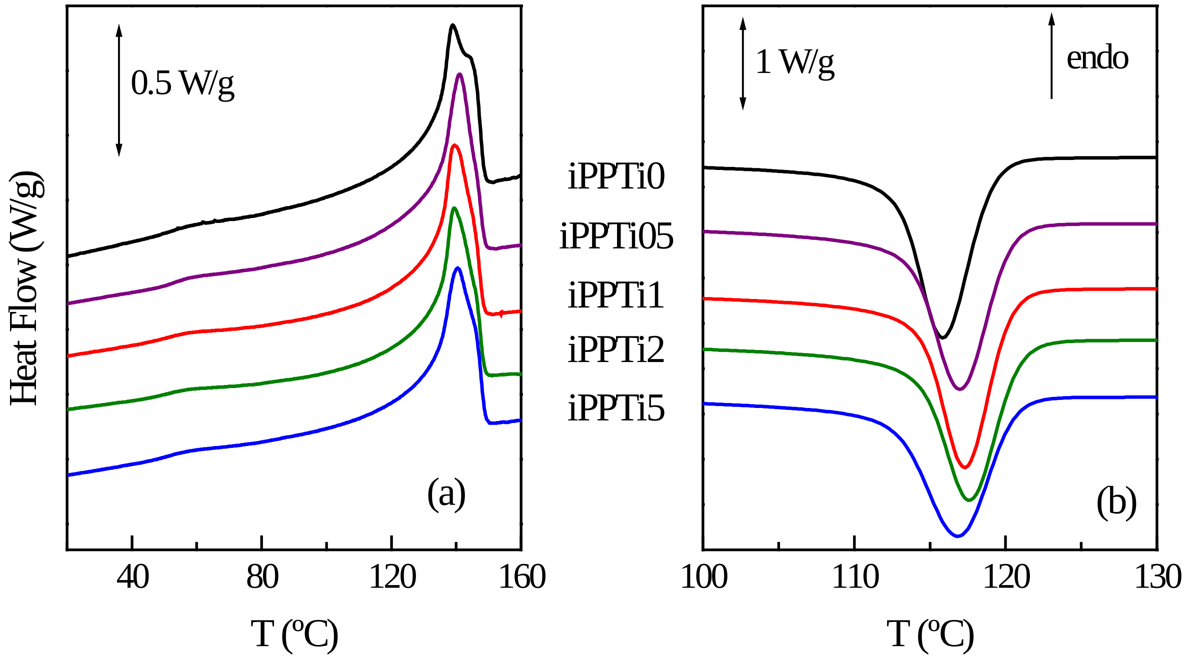

Figure 9. DSC curves corresponding to: (a) the first heating process and (b) the crystallization corresponding to the neat homopolymer and its nanocomposites with distinct TiO_2 nanoparticle contents.

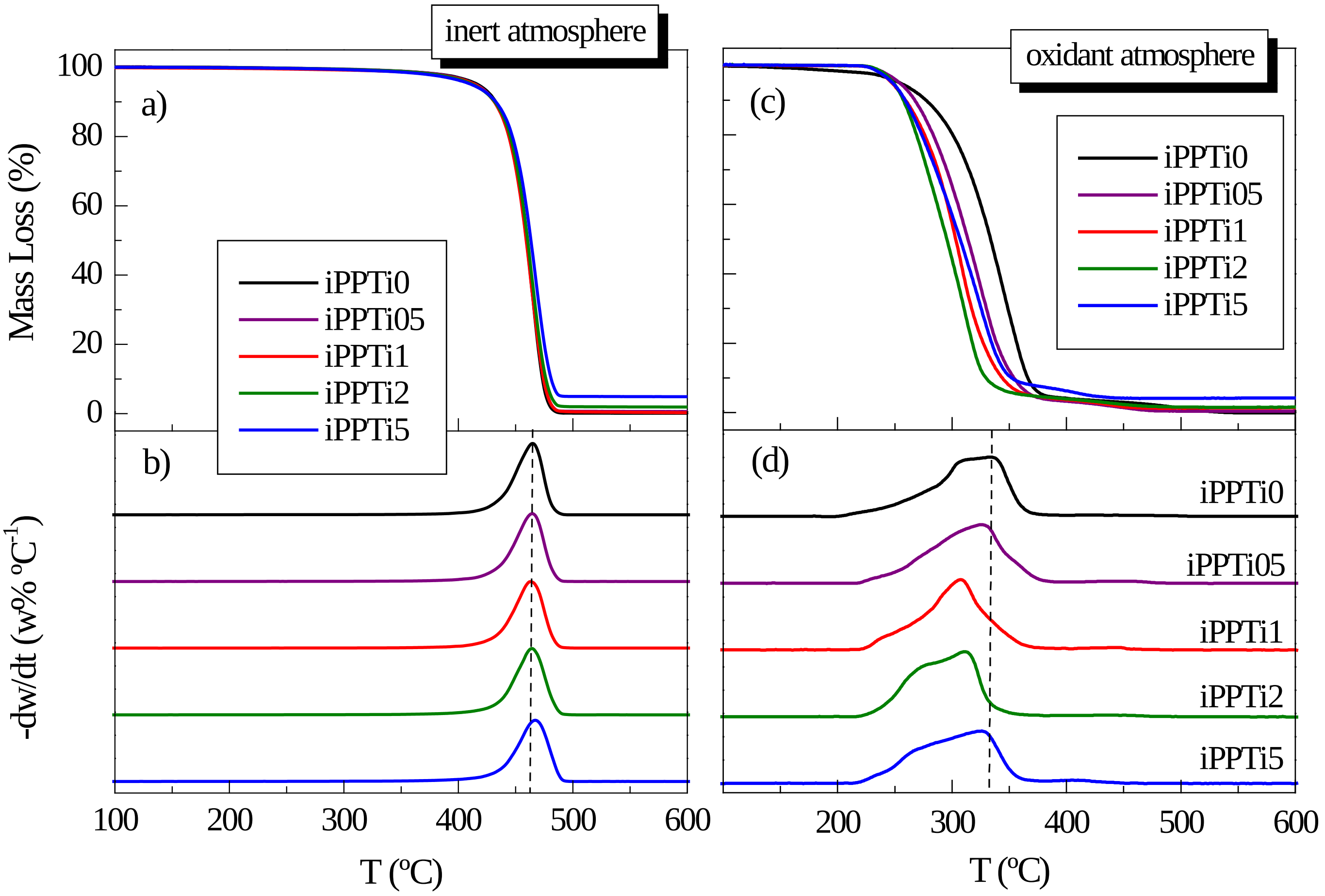

Figure 10. Left plot: (a) TG and (b) DTG curves obtained under an inert atmosphere; Right plot: (c) TG and (d) DTG curves obtained under an oxidant atmosphere of neat homopolymer and the different nanocomposites analyzed. DTG curves have been vertically shifted for clarity.

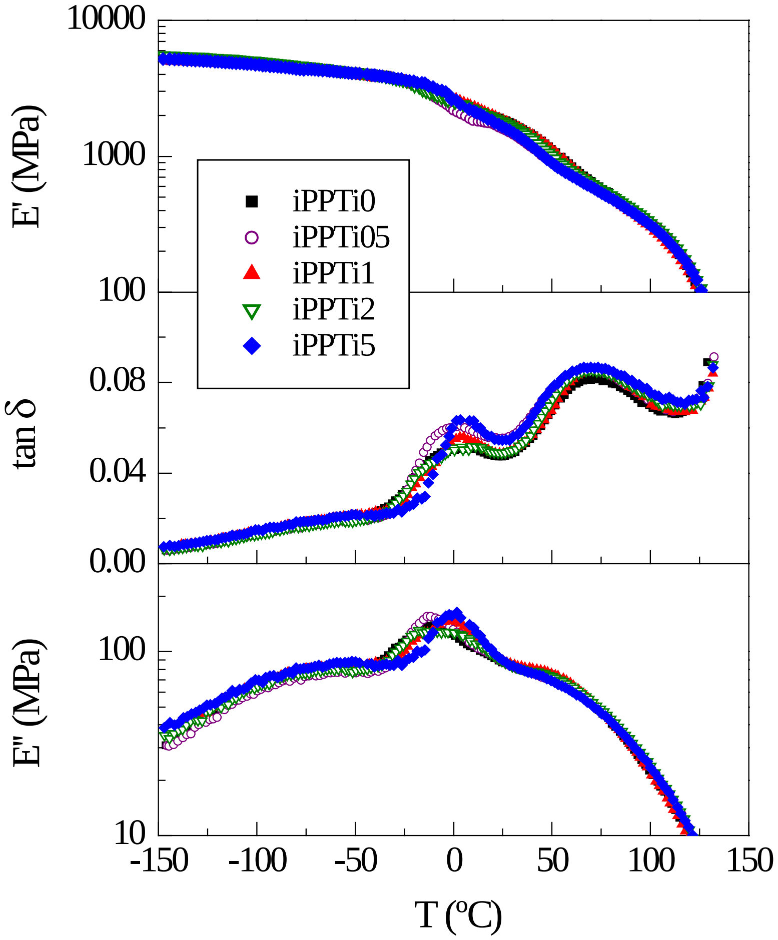

Figure 11. Temperature dependence of the two components to the complex modulus (EN and E″) and of the loss tangent (tan δ) for the neat homopolymer and its nanocomposites with distinct TiO_2 nanoparticle contents.

References

[1] Matsunaga T, Tomoda R, Nakajima T, Wake H. FEMS Microbiol Lett 1985;29:211-214.

[2] Joo J, Kwon SG, Yu T, Cho M, Lee J, Yoon J, Hyeon T. J Phys Chem B 2005;109: 15297-15302.

[3] Kubacka A, Cerrada ML, Serrano C, Fernandez-Garcia M, Ferrer M, Fernandez-Garcia M. J Nanosci Nanotechnol 2008;8:3241-3246.

[4] Cerrada ML, Serrano C, Sánchez-Chaves M, Fernández-García M, de Andrés A, Riobóo R J, Fernández-Martín F, Kubacka A, Ferrer M, Fernández-García M. Environ Sci Technol 2009;43:1630-1634.

[5] Kubacka A, Ferrer M, Cerrada ML, Serrano C, Sánchez-Chaves M, Fernández-García M, de Andrés A, Riobóo R J J, Fernández-Martín F, Fernández-García M. Appl Catal B 2009;89:441-447.

[6] Kubacka A, Serrano C, Ferrer M, Lunsdorf H, Bielecki P, Cerrada ML, Fernandez-Garcia M; Fernandez-Garcia M. Nano Lett 2007;7:2529-2534.

[7] Cerrada ML, Serrano C, Sánchez-Chaves M, Fernández-García M, Fernández-Martín F, de Andrés A, Riobóo R J J, Kubacka A, Ferrer M, Fernández-García M. Adv Funct Mater 2008;18:1949-1960.

[8] Kubacka A, Cerrada ML, Serrano C, Fernández-García M, Ferrer M, Fernández-Garcia M. J Phys Chem C 2009;113:9182-9190.

[9] Jiménez Riobóo R J, Serrano-Selva C, Fernández-García M, Cerrada ML, Kubacka A, de Andrés A. J. Lumin. 2008;128:851-854.

[10] Thompson RB, Ginzburg VV, Matsen MW, Balazs AC. Science 2001;292:2469-2472.

[11] Mackay ME, Tuteja A, Duxbury PM, Hawker CJ, Van Horn B, Guan Z, Chen G, Krishnan RS. Science 2006;311:1740-1743.

[12] Warren SC, DiSalvo FJ, Wiesner U. Nat Mater 6;2007:156-161.

[13] Mackay M E, Dao TT, Tuteja A, Ho DL, Van Horn B, Kim HC, Hawker CJ. Nat Mater 2003;2:762-766.

[14] Bansal A, Yang H, Li C, Cho K, Benicewicz BC, Kumar SK, Schadler LS. Nat Mater 2005;4:693-698.

[15] Narayanan RA, Thiyagarajan P, Lewis S, Bansal A, Schadler LS, Lurio LB. Phys Rev Lett 2006;97:075505/1-075505/4

[16] Ferry J D. *Viscoelastic properties of polymers.* New York: John Wiley and Sons 1980.

[17] Mansel S, Pérez E, Benavente R, Pereña JM, Bello A, Röll W, Kirsten R, Beck S, Brintzinger HH. Macromol Chem Phys 1999;200:1292-1297.

[18] Wunderlich B. *Macromolecular Physics* vol 3, New York: Academic Press 1980.

[19] Smith GD, Bedrov D, Li L, Byutner O. J Chem Phys 2002;117:9478-9489.

[20] Bahloul W, Bounor-Legaré V, David L, Cassagnau P. J Polym Sci, Part B: Polym Phys 2010;48:1213-1222.

[21] Bartholome C, Beyou E, Bourgeat-Lami E, Cassagnau P, Chaumont P, David L, Zydowicz N. Polymer 2005;46:9965–9973.

[22] Natta G, Corradini P. Il Nuovo Cimento 1960;15:40-51.

[23] Krache R, Benavente R, López-Majada JM, Pereña JM, Cerrada ML, Pérez E. Macromolecules 2007;40:6871-6878.

[24] Turner-Jones A. Polymer 1971;12:487-508.

[25] Arranz-Andrés J, Benavente R, Pérez E, Cerrada ML. Polym J 2003;35:766-777.

[26] Cerrada ML, Pérez E, Benavente R, Ressia J, Sarmoria C, Vallés EM. Degrad. Stab. 2010;95:462-469.

[27] Alamo RG., Kim M-H, Galante MJ, Isasi JR, Mandelkern L. Macromolecules 1999;32:4050-4064.
[28] Palza H, López-Majada JM, Quijada R, Benavente R, Pérez E, Cerrada ML. Macromol Chem Phys 2005;206:1221-1230.
[29] López-Majada JM, Palza H, Guevara JL, Quijada R, Martínez MC, Benavente R, Pereña JM, Pérez E, Cerrada ML. J Polym Sci, Part B: Polym Phys 2006;44:1253-1267.
[30] Arranz-Andrés J, Peña B, Benavente R, Pérez E, Cerrada ML. Eur Polym J 2007;43:2357-2370.
[31] Baltá-Calleja FJ, Vonk CG. *X-Ray Scattering of Synthetic Polymers*. Amsterdam: Elservier 1989.
[32] Ryan AJ, Stanford JL, Bras W, Nye TMW. Polymer 1997;38:759-768.
[33] Crist B. J Polym Sci, Part B: Polym Phys 2001;39:2454-2460.
[34] Jourdan C, Cavaille JY, Perez J. J Polym Sci, Part B: Polym Phys 1989;27:2361-2384.
[35] Rotter G, Ishida H. Macromolecules 1992;25:2170-2176.